

UiO-66-NH₂ Metal–Organic Frameworks with Embedded MoS₂ Nanoflakes for Visible-Light-Mediated H₂ and O₂ Evolution

Satyabrata Subudhi, Gayatri Swain, Suraj Prakash Tripathy, and Kulamani Parida*

Cite This: <https://dx.doi.org/10.1021/acs.inorgchem.0c01030>

Read Online

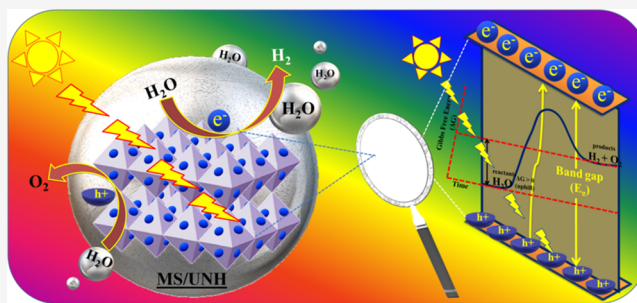
ACCESS |

Metrics & More

Article Recommendations

Supporting Information

ABSTRACT: Hydrogen evolution from water splitting by means of a photocatalytic approach is an ideal future energy source and free of fossil reserves, in contrary photocatalytic O₂ evolution remains a bottleneck due to high over potential and low efficiency. For reasonable use of solar light, photocatalysts must be sufficiently stable and efficient toward harvesting of sunlight from both theoretical and practical viewpoints. In this regard, here we have prepared MoS₂-modified UiO-66-NH₂ MOF through a facile hydrothermal technique and evaluated its efficiency toward photocatalytic H₂ and O₂ evolution by water splitting in the presence of sacrificial agents. A couple of similar type of analyses have been studied previously; however, this analysis represents a diverse scientific approach on the basis of interfacial contact toward reveal the actual potential of nanoflakes MoS₂ as well as UiO-66-NH₂. In this regard the as-synthesized photocatalyst was well-characterized by XRD, FTIR, UV–vis diffuse reflectance spectra, FESEM, HRTEM, XPS, and BET analysis techniques, which provide sufficient evidence toward successful synthesis of the pristine materials and efficacious anchorage of MoS₂ on the active surface of UiO-66-NH₂ by the ionic interaction between Zr–O and S/Mo. Among the synthesized photocatalysts (3 wt %) MoS₂/UiO-66-NH₂ shows the optimum outcome toward H₂ and O₂ evolution, i.e., 512.9 μmol/h (4.37 times greater than bare UiO-66-NH₂) and 263.6 μmol/h (4.25 and 11.32 times greater than bare UiO-66-NH₂ and MoS₂, respectively). The superior performance obtained by the composite is due to the synergistic effect of pristine UiO-66-NH₂ and MoS₂ which proceeds through a type-II interband alignment for the facile channelization of excitons. This investigation will bestow a beneficial blue-print to construct challenging photocatalysts and to find out the paramount performance toward photocatalytic water redox reaction.



1. INTRODUCTION

Water splitting facilitates cleavage of H–O–H bond by different energy source, i.e., electrical (electrolysis), thermal (thermolysis), or light (photolysis). Among these methods, the photolysis of water in the presence of a photocatalyst can be treated as a promising technique for both H₂ and O₂ evolution in which the most important criteria is the alignment of redox potential of water with electronic bandgap of photocatalyst.¹ The conversion of photon energy to chemical energy in the presence of heterogeneous photocatalyst by the photo-induced decomposition of H₂O has attracted global attention as an ecofriendly method to mitigate future energy catastrophe and environmental issues. It is quite difficult to achieve one-pot water splitting under visible-light illumination due to uphill nature of the reaction, so sacrificial reagents such as methanol or silver nitrates are used as hole or electron scavenger, respectively, to evaluate the photocatalytic activity of the photocatalyst.^{2,3} In this regard, photocatalyst should fulfill the thermodynamic requisites during each half cell reaction (hydrogen and oxygen evolution) of photocatalytic water splitting, i.e., the valence band (VB) potential must be more positive than water oxidation potential (H₂O/O₂ = 0.82 V, pH 7) and the conduction band potential must be more negative

than water reduction potential (H⁺/H₂ = −0.41 V, pH 7).⁴ Therefore, the exploitation of visible-light active photocatalyst is very important for effective absorption and conversion of solar energy for environmental remediation. Despite the great efforts devoted to design highly efficient photocatalysts, the photocatalytic results are significantly limited due to narrow light absorption and swift electron–hole recombination. In this regard, the development of heterojunction (basically p–n heterojunction)-based photocatalyst has garnered more attention to resolve these issues due to its effective electron–hole anti-recombination capabilities.⁵

In this aspect, metal–organic framework (also called porous coordination polymers (PCPs)) are regarded as an interesting type of porous hybrid crystalline material due to its flexible porosity and viability for post-synthetic modification. These

Received: April 8, 2020

features formulate MOF as an efficient candidate toward various applications such as gas storage and separation, membrane separation technology of various wastewater, chemical sensing, drug delivery, and catalytic transformation of organic molecules.^{6–8} In order to get water-stable and visible-light-active MOF, two common strategies are applied, i.e., (i) introduction of functional group ($-\text{NH}_2$, $-\text{SH}$) based linker as the bridging unit with metal clusters on the basis of hard/soft acid/base (HSAB) principle and (ii) heterojunction with visible-light-active photocatalyst.^{6,8–10} In the current study, we have employed both the approach to make a suitable and efficient photocatalyst. From the viewpoint of band structure, the conduction band (CB) of MOF is constructed by the empty outer orbitals of the metal center, and the valence band is mainly contributed to by the outer orbitals of organic linkers. The linker effectively absorbs solar light and transfers the energy to the metal center, which is termed ligand to cluster/metal charge transfer (LCCT/LMCT).¹¹ Moreover MOFs exhibited a suitable band gap as well as a reasonable band edge potential which are the two fundamental requirements for water redox reaction and possesses long-term stability against photocorrosion under light illumination in aqueous solution.^{12–18} Mori's group has first employed MOF toward the hydrogen evolution reaction. Garcia et al.¹⁹ reported water splitting by Zr-based MOFs such as UiO-66 and UiO-66-NH₂ for first time under UV-light illumination in 2010. Lin et al.²⁰ has carried out the visible-light-driven H₂ evolution reaction by incorporating Pt in the active pores of MOFs. Rosseinsky et al.²¹ has carried out H₂ evolution reaction by Al-containing porphyrin MOF. However, the outcomes of these experiments were not up to the mark. Afterward, most efforts have been focused to enhance the photocatalytic activity of MOF by coupling with plasmonic metals and doping with metals/nonmetals by hydrothermal method.²²

The researchers has also provide their immense attention toward metal sulfide systems, i.e., basically toward MoS₂ (MS)^{23,24} in the field of electrocatalysis, pollutant degradation, and so on. MoS₂ is an intrinsically p-type semiconductor and is generally arranged in a way such that the hexagonally packed 6-fold coordinated Mo atoms are covalently bonded with two atomic layers of trigonal chalcogens in a S–Mo–S fashion. The S–Mo–S layers were bonded with each other by weak van der Waal's forces of attraction. The suitable molecular arrangement and good crystalline property is unable to resolve unsatisfactory the photocatalytic property which is mainly due to low charge carrier density as well as low conductivity between the adjacent S–Mo–S layers of MS.²⁵ However, when it is coordinated with any other photocatalyst it then enhances the light-absorption capacity and charge separation efficiency of the primary photocatalyst to a greater extent. Various works have been proposed in this regard, such as MoS₂/CdS, MoS₂/CeO₂, MoS₂/CaIn₂S₄, and MoS₂/g-C₃N₄.^{26,27}

It is well-known that both MoS₂ (MS) and UiO-66-NH₂ (UNH) have suitable band edge potential, yet their unaided utilization shows less efficiency toward the water redox reaction due to high charge recombination. However, their heterostructure composite can work as a promising photocatalyst with enhanced activity. Hao et al. and Shen et al. reported EY-sensitized MoS₂ QDs/UiO-66-NH₂/G and MoS₂/UiO-66/CdS hybrid with enhanced photocatalytic activity toward H₂ evolution,^{28,29} as presented in Table 1; however, the quaternary and tertiary junctions make the

Table 1. Performed Photocatalytic Applications of MoS₂-Based UiO-66-NH₂ Photocatalyst

	photocatalyst	photocatalytic activity in the presence of 300 W xenon lamp (light source)		
		H ₂ evolution	O ₂ evolution	time
1	EY-sensitized 5 wt % MoS ₂ QDs/UiO-66-NH ₂ /G	186.37 μmol		3 h
2	1.5 wt % MoS ₂ /UiO-66/CdS	650 μmol		1 h
3	3 wt % MoS ₂ /UiO-66-NH ₂ (present work)	512.9 μmol	263.6 μmol	1 h

composite very complicated. In this work, we have reported nanoflakes MoS₂ embedded UiO-66-NH₂ (MS/UNH)-based heterojunction with intermediate weight percent variation of MoS₂ in comparison to previous works and study its application toward photocatalytic H₂ evolution and O₂ evolution reactions. The analysis outcome shows superior activity in comparison to EY-sensitized MoS₂ QDs/UiO-66-NH₂/G photocatalyst and almost equivalent activity in comparison to that of the MoS₂/UiO-66/CdS photocatalyst. The science behind the augmented photocatalytic activity is mainly attributed to the surface contact of coupled photocatalyst as well as the availability of the active surface of the formed composite toward photocatalytic reaction. The successful interaction between nanoflake MS and UNH facilitates the photoabsorption potential as well as the photostability of the material, thus suppressing the photoexciton recombination. The successful interaction provides a type-II interband alignment in which the internal electric field created at the junction of two material causes separation of photogenerated charge carriers more efficiently thus enhancing the photocatalytic activity. Thus, the as-synthesized MS/UNH would open up a new direction in MOF-based heterojunctions toward various environmental photocatalytic applications under visible-light irradiation.

2. EXPERIMENTAL SECTION

2.1. Chemicals Utilized. Zirconium chloride (ZrCl₄), 2-amino-1,4-benzene dicarboxylic acid (H₂BDC-NH₂), sodium molybdate (Na₂MoO₄·2H₂O), and thiourea (CH₄N₂S) were purchased from sigma Aldrich. Methanol, ethanol, and *N,N*-dimethylformamide (DMF) were obtained from Merck and were used without further purification.

2.2. Synthesis of UNH. UiO-66-NH₂ photocatalyst was synthesized via hydrothermal method as reported previously.³⁰ In a typical preparation procedure, equimolar amounts (7 mmol) of zirconium chloride and 2-amino terephthalic acid (ATA) were stirred separately in DMF (40 mL) solution for 30 min. The formed zirconium chloride and ATA solutions were mixed and was stirred for more 30 min. Then, so formed suspension solution was undergo for hydrothermal treatment for 24 h at 120 °C. After the time, is over it was cooled to room temperature, and the sample was alienated via centrifugation. Next, the sample was rinsed several times with methanol to eliminate the remaining unreacted metal salts/organic moieties. For pore activation, it was kept in methanol for 72 h and was separated by centrifugation followed by drying at 100 °C for 12 h, and the obtained product was named UiO-66-NH₂ (UNH).

2.3. Synthesis of MS. Pristine MoS₂ was synthesized by hydrothermal method as reported previously.²⁶ In a typical preparation procedure, 1:5 mmol sodium molybdate and thiourea were stirred separately in 80 mL of EtOH/H₂O (1:3) solution and were sonicated for 30 min followed by constant stirring for 30 min. Then, the so-formed suspension solution was undergo for hydro-

Scheme 1. Schematic Representation of the Synthesized (i) MS, (ii) UNH, and (iii) MS/UNH (1, 3, and 5 wt %)

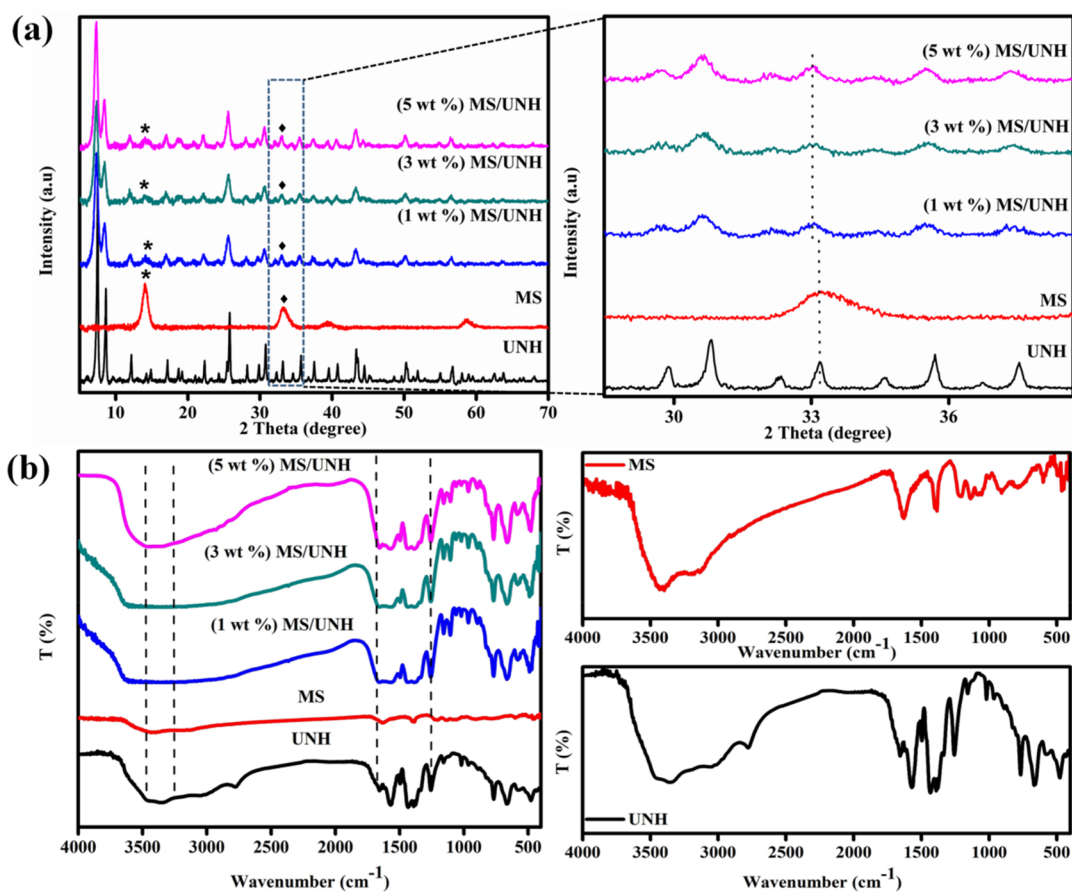
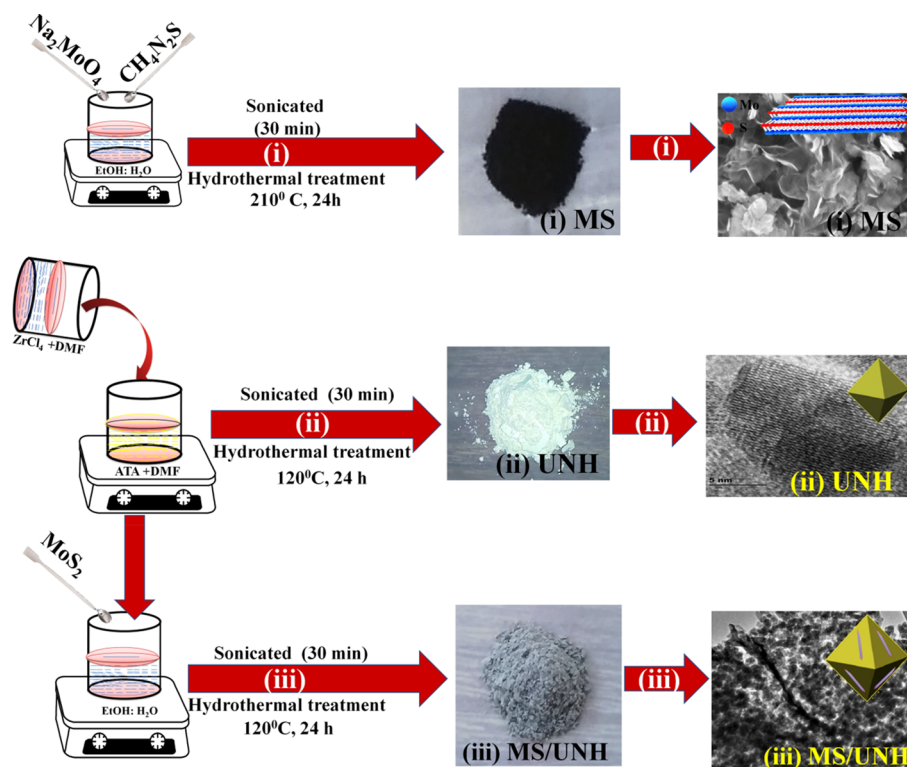


Figure 1. (a) XRD and (b) FTIR of UNH, MS, and MS/UNH (1, 3, and 5 wt %)

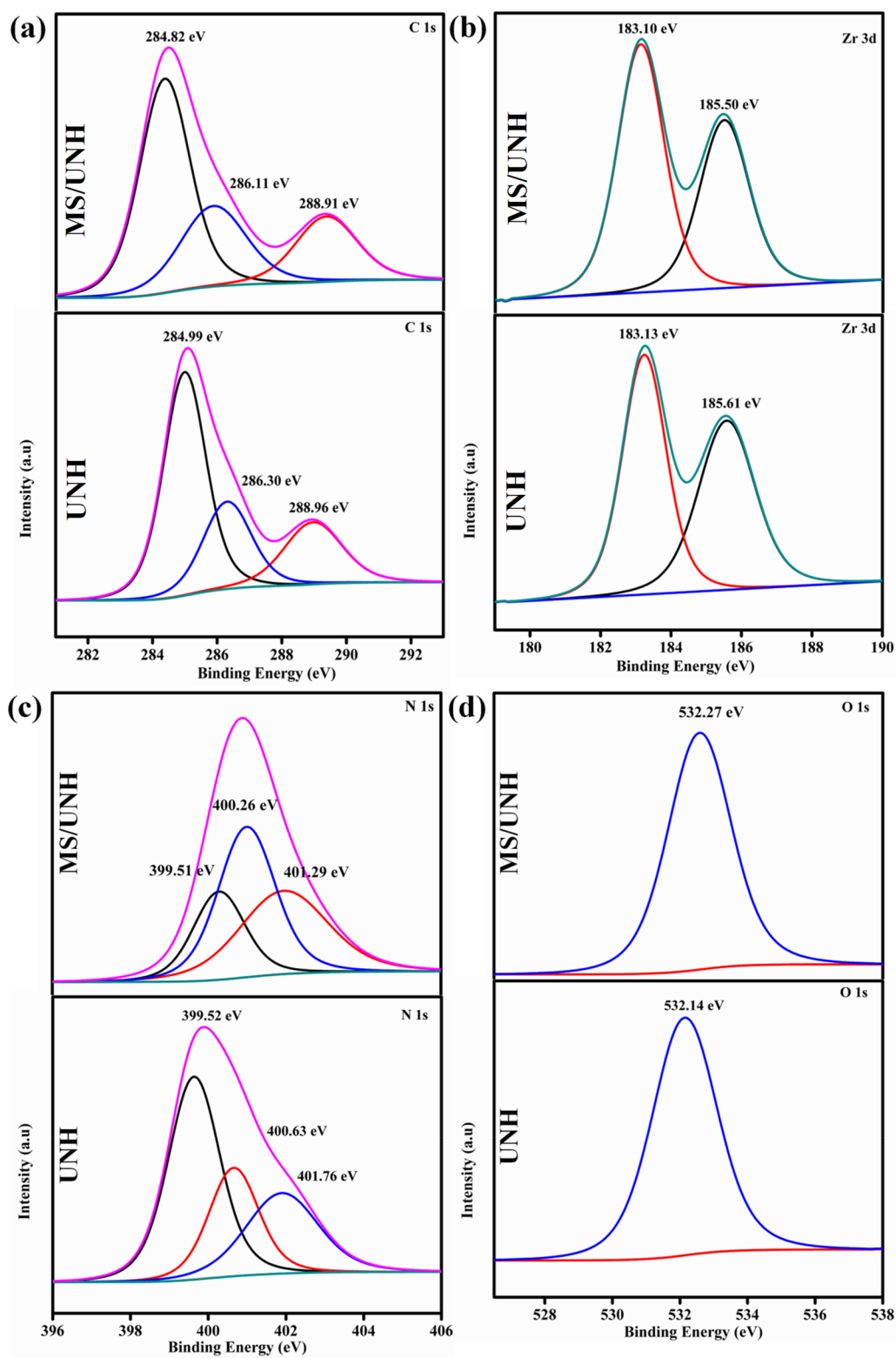


Figure 2. continued

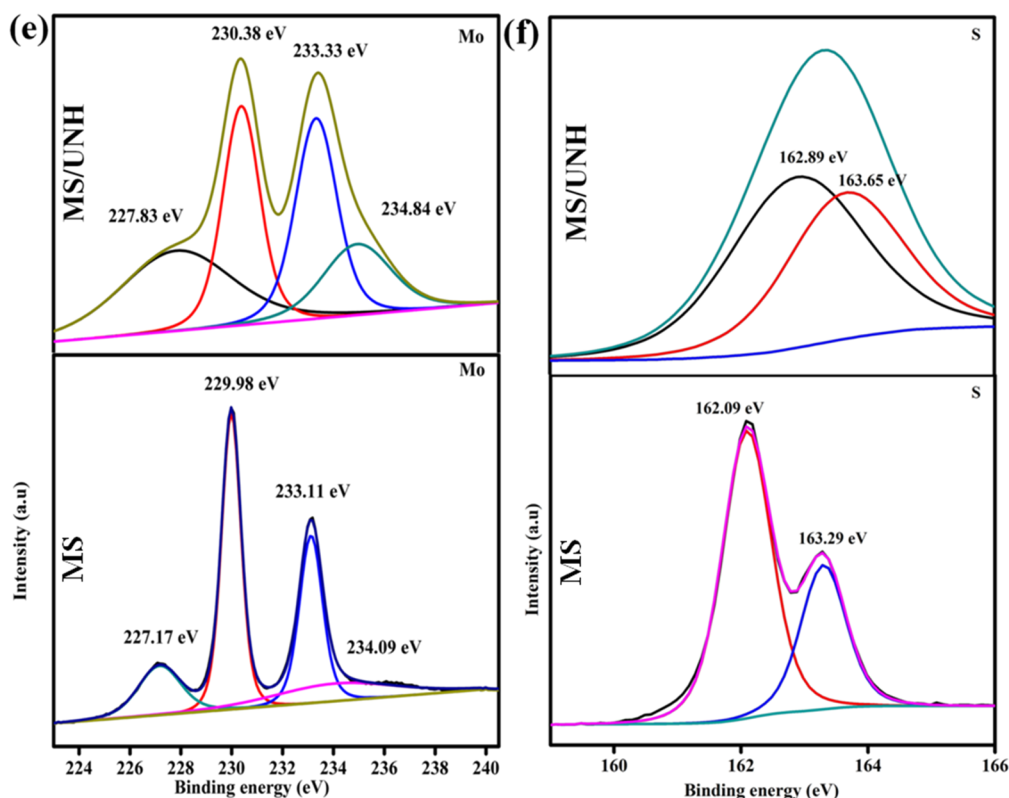


Figure 2. XPS peaks of (a) C 1s, (b) Zr 3d, (c) N 1s, (d) O 1s, (e) Mo 3d, and (f) S 2p.

thermal treatment by a Teflon-lined stainless-steel autoclave for 24 h at 210 °C. After the time is over, it was cooled at room temperature, and the sample was alienated via centrifugation. Then, the sample was rinsed three times with the EtOH/H₂O (1:3) solution. It was oven-dried at 80 °C for 12 h, and the obtained product was named MoS₂ (MS).

2.4. Synthesis of MS/UNH. MS/UNH heterojunction photocatalyst was prepared by adding as prepared MS in required weight percentage during UNH synthesis as described above. This procedure was followed to prepare three composites, i.e., MS/UNH (1, 3, and 5 wt %), by weight percent variation of MS. The detailed synthesis method is illustrated in Scheme 1.

3. PHOTOCATALYTIC EXPERIMENTAL ANALYSIS FOR WATER SPLITTING

The photocatalytic efficiency of the as synthesized photocatalysts was tested toward water redox reaction by using a sealed quartz batch reactor containing 0.02 g of the photocatalyst in 20 mL of various scavengers. For the H₂ evolution reaction, a 10% methanol solution was used, whereas 0.05 M AgNO₃ solutions were used for the O₂ evolution reaction. The solution was stirred to prohibit the coagulation in the presence of 300 W Xe arc lamp (cutoff filter > 420 nm) as a visible-light source. The Xe arc lamp was kept 8.7 cm away from the reaction solution. Prior to the initiation of the photocatalytic reaction, the suspension solution was treated with N₂ gas for 1 h to remove the dissolved gases. The water displacement method was employed to collect the evolved H₂ and O₂ gas during the reaction and was analyzed with 5 Å molecular sieves and a thermal conductivity detector by GC analysis (Agilent Technology). Control photocatalytic experiments were carried out in absence of catalyst and light which show no result and confirm the importance of light and

catalyst. After 1 h of reaction, the H₂ and O₂ evolution by synthesized materials was depicted in the respective sections.

4. CHARACTERIZATION

4.1. Structural Characterization. XRD analysis of UNH, MS, and the series of MS/UNH were carried out to obtain the crystal structure and phase purity, as provided in Figure 1. The obtained result shows various sharp crystalline peaks for UNH and was well-matched with the reported literature values.²⁹ For MS, three sharp peaks were observed at 14.1, 33.3, and 58.9°. The peaks obtained at 14.1° represent the (002) diffraction peak,³⁰ which suggests the existence of a hexagonal phase of MS having lattice constants $a = b = 0.311$ and $c = 1.211$ and the space group $p63/mmc$.²⁶ Moreover, the XRD analysis concluded that there is no impurity in crystal lattice. In composites, the peak intensity decreases, and blue-shifting was observed in comparison to both UNH and MS as depicted in Figure 1a. The decrease and shifting in peak positions well represents the coordination of MS with UNH in MS/UNH photocatalyst. Moreover, the presence of MS peaks also indicates the fabrication of MS on exposed surface of UNH instead of open pores and was further verified from FESEM analysis as depicted in respective sections. Additionally, FTIR analysis was carried out to study various vibrational modes of the functional group present in the photocatalyst as shown in Figure 1b. The broad and sharp bands at 1626 and 3432 cm⁻¹ represent the bending and stretching vibration of the H–O–H linkage.³¹ The peak at 467 cm⁻¹ represents the characteristic Mo–S stretching vibration.³² In addition, the peak at 3477 and 3340 cm⁻¹ represents the stretching frequency for asymmetric and symmetric vibration of –NH₂ group of UNH. The peaks at 1642 cm⁻¹ represents the N–H bending vibration, and the peak at 1244 cm⁻¹ denotes the C–N stretching of aromatic

Table 2. XPS Analysis of UNH, MS, and MS/UNH

		binding energy			ref
		C 1s			
UNH	288.96 eV	286.30 eV	284.99 eV		
MS/UNH	288.91 eV	286.11 eV	284.82 eV		34
difference	0.05 eV	0.19 eV	0.17 eV		
reason	(O=C–O) of ATA	C–NH ₂	C=C		
		N 1s			
UNH	401.76 eV	400.63 eV	399.52 eV		
MS/UNH	401.29 eV	400.26 eV	399.51 eV		35
difference	0.47 eV	0.37 eV	0.01 eV		
reason	=NH ₂ ⁺	–NH ₃ ⁺	–NH ₂		
		O 1s			
UNH	532.14 eV				
MS/UNH	532.04 eV				34
difference	0.10 eV				
reason	Zr–O bond				
		Zr 3d			
UNH	185.61 eV	183.13 eV			
MS/UNH	185.50 eV (3d _{3/2})	182.10 eV (3d _{5/2})			34
difference	0.11 eV	0.03 eV			
reason		Zr ⁴⁺			
		Mo 3d			
MS	227.17 eV	229.98 eV	233.11 eV	234.09 eV	
MS/UNH	227.83	230.38 eV (3d _{5/2})	233.33 eV (3d _{3/2})	234.84 eV	26
difference	0.66 eV	0.40 eV	0.22 eV	0.75 eV	
reason	(S 2S)	Mo ⁴⁺		Mo ⁶⁺	
		S 2p			
MS	162.09 eV	163.29 eV			
MS/UNH	162.89 eV (2p _{3/2})	163.65 eV (2p _{1/2})			26
difference	0.80 eV	0.36 eV			
reason		S ²⁻			

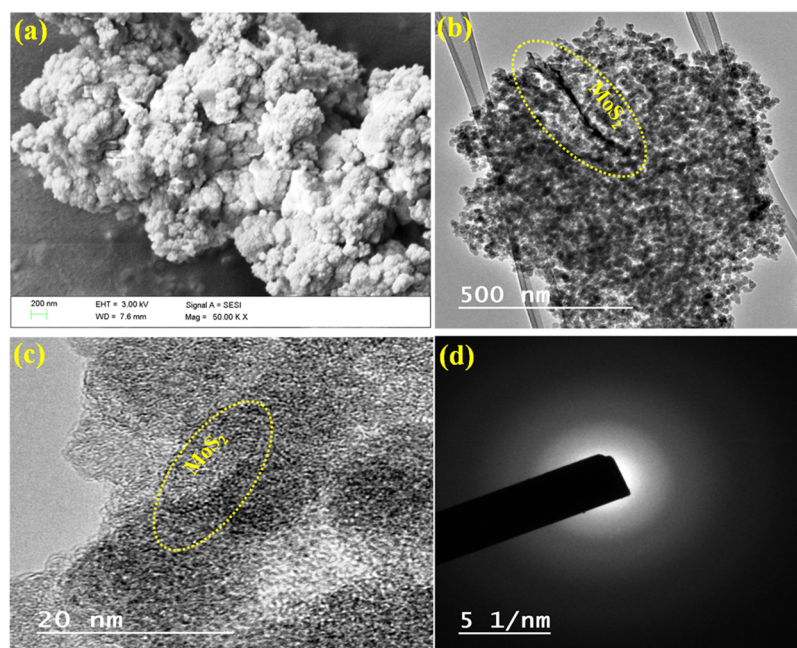


Figure 3. (a) FESEM image of MS/UNH, (b, c) HRTEM image of MS/UNH, (d) SAED pattern of MS/UNH

amines. A small band at 1510 cm^{-1} signifies the C=C moiety vibration of the aromatic ring. However, no eye-catching shifting was observed in any MS/UNH composite. The above observed FTIR data shows coupling between MS and UNH.

The architecture of heterojunction interface may inhibit the recombination of photogenerated excitons by their proper channelization and hence accelerate the surface reaction kinetics. The balanced alignment of energy bands estimates

the chemical characteristics of the heterojunction and consequently the deviation in energy states. Therefore, we have carried out high-resolution XPS analysis of UNH, MS, and MS/UNH to inspect the constituent elements with respect to their binding energy (BE) and the interfacial interaction between semiconductors which is depicted in Figure 2. In the first case, the variation in BE between UNH and MS/UNH was compared, in which the XPS spectra of C 1s disclosed three sharp peaks in both parent UNH (284.99, 286.30, and 288.96 eV) and MS/UNH (284.82, 286.11, and 288.91 eV) which are in good agreement with C=C, C-NH₂, and sp²-bonded carbonyl group of ATA, respectively. Similarly, the N 1s spectra of UNH are deconvoluted in to three peaks at 399.52, 400.63, and 401.76 eV that represent -NH₂, -NH₃, and =NH₂⁺ respectively, whereas for MS/UNH the -ve shifting in BE was observed as represented in Table 2. The BE of Zr is splitted in to two sharp peaks that represent the existence of Zr⁴⁺ states. Second, the variation in BE between MS and MS/UNH was compared, in which the XPS spectra of Mo was split in to four deconvoluted peaks at 227.83, 230.38, 233.33, and 234.84 eV for MS/UNH, in which the S 2s peak was located at 227.83 eV, and Mo⁴⁺ was represented by 3d_{5/2} and 3d_{3/2} spin state at BE 230.38 and 233.33 eV, respectively, and the Mo⁶⁺ state at 234.84 eV. S shows two deconvoluted peaks for 2p_{3/2} and 2p_{1/2} at 162.89 and 163.65 eV, respectively, that typically represent the existence of the S²⁻ state. This comparison analysis indicates that in composite MS/UNH the BE of Zr, N, and O has shifted toward a lower BE as compared to its pristine material, whereas the BEs of Mo and S of MS have shifted toward a positive BE as compared to its components present in neat MS. This opposite tendency indicates that after heterojunction formation the electron density increases on the surface of UNH, whereas it decreases at MS surface and confirms the channelization of photoexcited electrons from MS to UNH.³³ Additionally ICP-OES analysis result confirms existence of 0.97, 2.83, and 4.67 wt % of MS in MS/UNH (1, 3, and 5 wt %), respectively, and hence provides sufficient evidence about the stability of surface interaction between MS and UNH.

4.2. Morphological Characterization. **4.2.1. FESEM and HRTEM Analysis.** FESEM and HRTEM analysis of the synthesized photocatalyst were carried out to study the surface topology and elemental composition as depicted in Figure 3. The SEM image clearly illustrates that nanoflake MS were wrapped on the exposed surface of pristine UNH due to the strong interfacial contact. This intimate interaction may facilitate the fast transfer of photogenerated charge carriers and simultaneously inhibits the charge recombination rate which ultimately causes the enhancement of photocatalytic efficiency. The lattice fringe for UNH was not observed in the composite which is mainly due to the charging of nanoparticles under the influence of electron beam³⁶ and for MS the poor crystallinity might be the reason. However, the formation and morphology of pristine MS was confirmed from the FESEM and HRTEM analysis result as provided in Figure S1. Although the HRTEM images of MS/UNH composite does not contain any lattice fringes of MS, the existence of MS is clearly observed from the EDX analysis and color mapping data as provided in Figures S2 and S3. This demonstrates the presence and uniform distribution of Zr, Mo, S, C, N, and O elements in the composite.^{28,29} Moreover the SAED pattern (Figure 3d) of MS/UNH was provided in which the crystalline property was not observed due to the sensitivity of the UNH material

toward the electron beam. Moreover, the presence of above elements was further supported by XPS analysis in the respective section.

4.2.2. BET Analysis. The surface areas and pore volumes of UNH and MS/UNH were calculated from nitrogen adsorption–desorption isotherms analyzed by BET and BJH characterization techniques as shown in Figure 4. The obtained

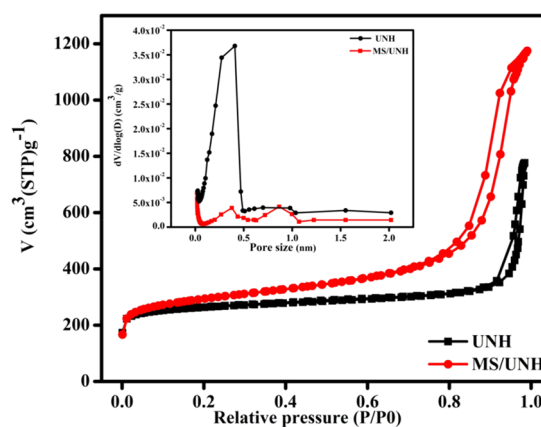


Figure 4. BET surface area and BJH pore volume distribution (inset) of UNH and MS/UNH (3 wt %).

graphical isotherm, i.e., a typical H3 hysteresis loop, demonstrates type-IV isotherms for both UNH and MS/UNH. The hysteresis loop appears for UNH at relative high pressure (p/p_0), which indicates the accumulation of pores.³⁶ The surface areas for UNH and MS/UNH were found to be 831.488 and 1017.36 m²/g, respectively. The increase in surface area in (3 wt %) MS/UNH in comparison to that of pristine UNH is might be due to the nanoflakes morphology of MS as provided in Figure S1. The observed enhanced surface area for 3 wt % MS/UNH reveals the important reason behind the higher photocatalytic activity. Moreover, BJH analysis result proves the presence of micropores in the as-synthesized pristine UNH and composite MS/UNH as shown in Figure 4 (inset). However, after subsequent modification with MS, the pattern of the isotherm was preserved, and the pore size remains constant. However a slight decrease in pore volume was observed (UNH = 0.40 and 0.97 nm, MS/UNH = 0.38 and 0.87 nm). As it is well-observed from the SEM and HRTEM analysis that MS does not occupy any pores of UNH and only integrated on the surface of pristine UNH; hence, the decrease in pore volume may be due to the presence of trapped recrystallized ATA residue in the pores of UNH. In brief, the increase in surface area is due to the close electrostatic interaction of Zr with Mo–S group that increases the active surface of the pristine UNH. Although MS loading causes the increase in surface area and consequently increases the photocatalytic activity, the 5 wt % composite shows less catalytic activity in comparison to the 3 wt % composite which might be due to wrapping of the active surface of UNH by agglomeration and hence leads to its less availability toward participation in photocatalytic reactions.

4.3. Optical Characterization. A comparative study of UV–vis diffuse reflectance spectra (DRS) spectra of the synthesized photocatalysts has been depicted in Figure 5. The observed data shows that there is a continuous red shift in the absorption edges with gradual increase in the weight percentage of MS as observed for MS/UNH composite,

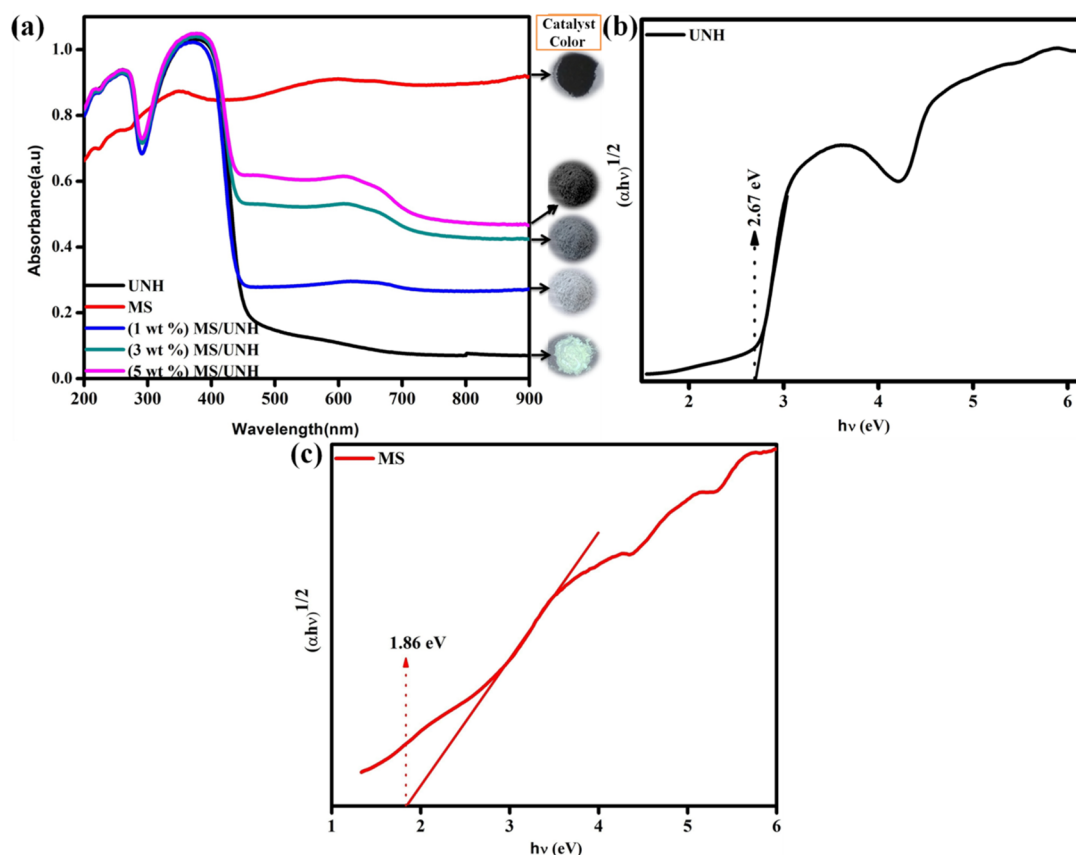


Figure 5. (a) Diffuse reflectance spectra of UNH, MS, and MS/UNH (1, 3, and 5 wt %). (b) Tauc plot of UNH. (c) Tauc plot of MS.

which implies that the band gap was precisely controlled according to the variation of molar ratio of MS. There is also a change in color from yellow to dark brown was observed with the increasing weight percentage of MS for the prepared composite which might reduce the reflection of light and increases the absorption capacity of visible light as observed in UV–vis spectra. The band gap energy for UNH and MS were observed as 2.67 and 1.86 eV by extrapolating the straight portion of $(\alpha h\nu)^{1/2}$ versus photon energy ($h\nu$) according to the Kubelka–Munk equation from the UV–vis diffuse spectra as depicted in eq 1.

$$\alpha h\nu = A(h\nu - E_g)^{n/2} \quad (1)$$

where α = proportionality constant, h = planks constant, ν = frequency of light, A = absorption coefficient, E_g = band gap, and n = type of electronic transition.

Moreover, the band gap observed for composite 3 wt % MS/UNH was 2.55 eV. This narrower band gap not only increases the photon absorption capacity but also promotes the lifetime of active species (e^- and h^+) which is well-supported by photoluminescence (PL) analysis as shown in Figure S4 and has been explained in a separate section. Except for band gap, the finding of band edge potential is very important to estimate the catalytic potential toward proposed applications. After getting the corresponding VB and CB for UNH and MS, their complementary band edge potentials were calculated from the UV–vis analysis by applying the eq 2 as follows:

$$E_g = VB - CB \quad (2)$$

Moreover, the UV–vis spectrum shows two sharp bands for UNH at 265 nm for $n-\pi^*$ transition of amino group of 2-ATA

and at 365 nm for $\pi-\pi^*$ transition of ATA and Zr–O cluster. The broad band observed at around 578 and 676 nm for MS corresponds to k - and k' -point of Brillouin's zone, which can be observed in MS/UNH and provides sufficient evidence about the chemical interaction between the parent entities.^{32,37,38}

4.4. Electrochemical Characterization. Electrochemical analysis is an important analytical technique that uses electrical stimulation to study the chemical reactivity of the photocatalyst. More specifically it analyses the redox reactions that provides vital information related to kinetics and mechanism of the reaction.

EIS analyses of the photocatalyst were carried out to analyze charge transfer activity as well as interfacial charge migration resistance. As is well-known, the smaller the arc diameter of Nyquist plot, the higher the charge separation efficiency, leading to superior electrical conductivity. In the present investigation, a smaller arc was formed by (3 wt %) MS/UNH in comparison to that of parent UNH, which indicates introduction of MS to UNH is very helpful to improve charge separation efficiency and hence its photocatalytic activity. In addition, current versus potential measurement (LSV) was further performed to investigate the photogenerated charge transfer and mechanism of the photocatalyst. The analysis was carried out for parent UNH, MS, and MS/UNH at 5 mV s^{-1} in an appropriate potential range as depicted in Figure 6b. The LSV spectrogram reveals the p- and n-type semiconductor character of MS and UNH, respectively. However, MS/UNH shows both cathodic and anodic characteristics with enhanced current density which represents the successful formation of p–n heterojunction architecture by the composite.

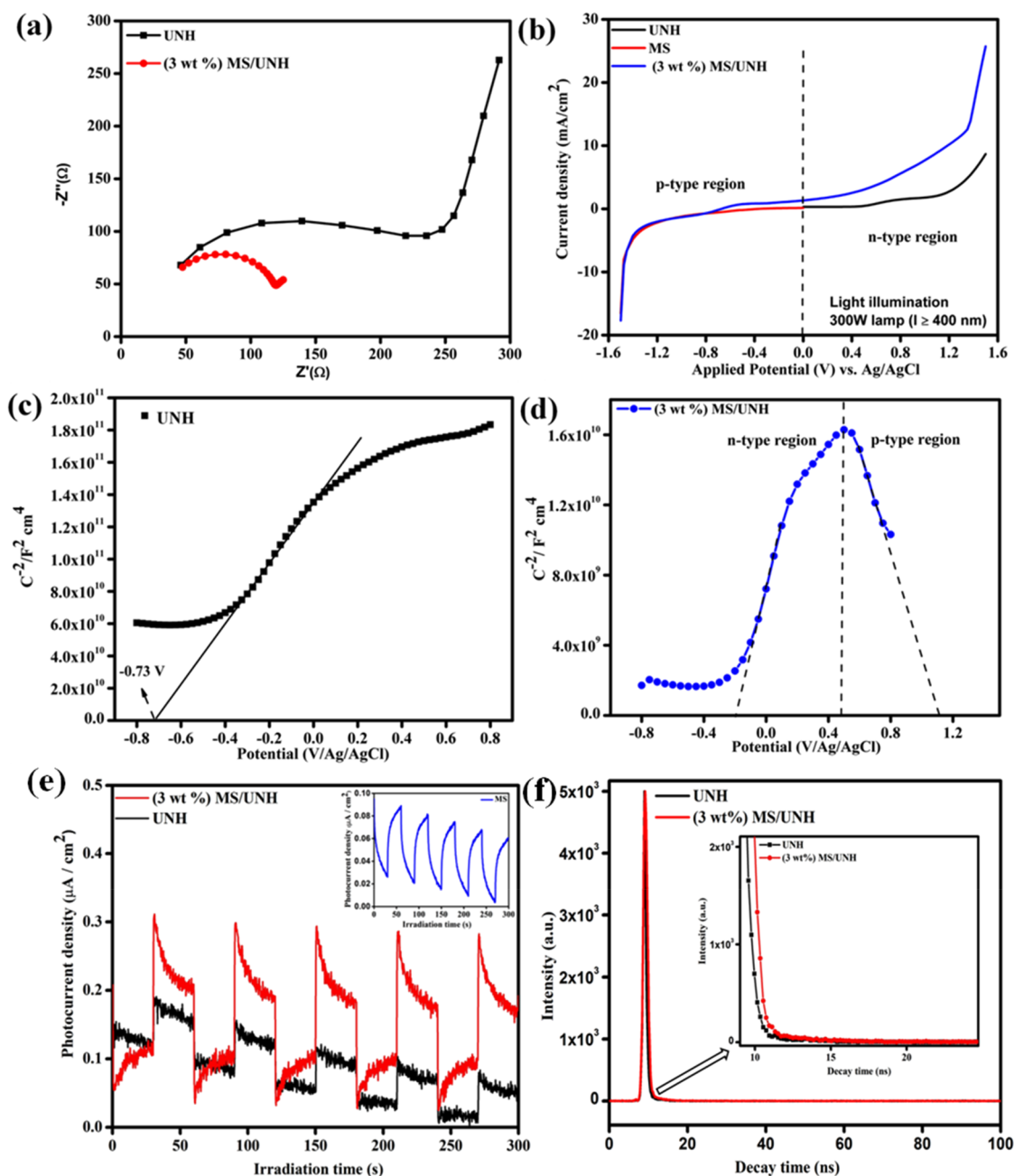


Figure 6. (a) EIS representation. (b) LSV representation of UNH, MS, and (3 wt %) MS/UNH. (c, d) Mott–Schottky representation of UNH and (3 wt %) MS/UNH. (e) Transient photocurrent representation of UNH, M, and (3 wt %) MS/UNH. (f) TRPL representation of UNH and (3 wt %) MS/UNH.

Mott–Schottky analysis was carried out to determine the electronic band structure, band edge potential, and hence the charge transfer pathway to propose the photocatalytic mechanism by the synthesized photocatalyst. In this regard, Mott–Schottky analysis was carried out in 0.2 M Na_2SO_4 for UNH and MS/UNH and 0.5 M H_2SO_4 for MS to learn the type of semiconductor catalyst (p-type/n-type). Figures 6d and S5) represents the Mott–Schottky spectrogram for parent UNH and MS with flat band potentials -0.73 and $+1.56$ V by drawing a tangent to the x -axis of the respective Mott–Schottky plot. Normally, the graph is plotted between the space charge capacitance (C_{SC}) versus applied potential (V_{app}) by using eq 3:

$$\Rightarrow C_{SC}^{-2} = \frac{2(V_{app} - V_{fb} - \frac{kT}{e})}{N_D \epsilon \epsilon_0 e A^2} \quad (3)$$

where k = Boltzmann's Constant, V_{fb} = flat band potential, T = absolute temperature, e = electric charge in C, N_D = donor density in cm^{-3} , ϵ and ϵ_0 = dielectric constant and dielectric constant in vacuum, and A = area in cm^2 .

After getting the flat band potential, the corresponding band edge potentials for MS were found to be $V_B = 1.78$ eV and $V_C = -0.08$ eV, and for UNH, these were found to be $V_B = 2.03$ eV and $V_C = -0.64$ eV by following eq 4:

$$\begin{aligned} &\Rightarrow E_{(\text{NHE}, \text{pH } 7)} \\ &= E_{\text{Ag}/\text{AgCl}} - 0.059 \times (7 - \text{pH of the electrolyte}) + 0.198 \end{aligned} \quad (4)$$

Moreover, the types of semiconducting character calculated for MS and UNH were p- and n-type, respectively, by following eqs 5 and 6:³⁵

$$\Rightarrow \frac{1}{C^2} = \frac{2}{q \in \infty N_a} \left(-E + E_{\text{fb}} - \frac{k_b T}{q} \right) \quad (\text{p-type}) \quad (5)$$

$$\Rightarrow \frac{1}{C^2} = \frac{2}{q \in \infty N_d} \left(E - E_{\text{fb}} - \frac{k_b T}{q} \right) \quad (\text{n-type}) \quad (6)$$

where k_b = Boltzmann's constant, T = absolute temperature, E = applied potential, N_d and N_a = donor density and acceptor density, respectively, C = space charge capacitance, and q = electronic charge, \in and ∞ = dielectric constant and dielectric constant in vacuum.

In the Mott–Schottky spectrogram, UNH shows a –ve spectrogram having a flat band potential of –0.73 V and that of MS shows a +ve spectrogram having a flat band potential of 1.56 V (Figure S5). The composite MS/UNH shows an inverted-V shape slope structure with corresponding +ve and –ve shifting in comparison to their pristine counterpart; hence, it indicates a higher donor density and better transfer of charge carrier efficiency. Furthermore, the positive shifting in the flat band potential of both UNH and MS implies the bending of corresponding band edges to facilitate the transfer of charge carriers at the heterojunction interface and further proves the formation of p–n heterojunction architecture by the composite.

Transient photo current response for UNH, MS, and (3 wt %) MS/UNH was characterized with several on–off cycles under visible-light irradiation, to investigate the separation efficiency of photoexcited charge carriers as depicted in Figure 6e. As photocurrent is mainly due to diffusion of photo-generated electrons to the back contact, in the meantime holes are taken up by the hole acceptor in the electrolyte.^{39,40} The smallest photocurrent density for pristine MS (inset) and UNH represents rapid recombination of photogenerated electron–hole pairs; however, comparatively higher photocurrent density of (3 wt %) MS/UNH represents the superior lifetime of photogenerated electron–hole pairs in p–n junction material.⁴¹ Moreover, this experiment provides adequate evidence of effective exciton separation and suppressed recombination of electron–hole pairs after the introduction of MS in UNH due to interfacial interaction by p–n heterojunction formation.

Moreover, the stability of photogenerated active species was further supported by PL spectroscopy experiment, which was carried out at room temperature with an excitation wavelength of 360 nm. The less intense PL intensity for the composite MS/UNH represents good exciton separation, superior charge transfer, and recombination inhibition in comparison to pristine UNH which is well matched with the observed photocatalytic activity results. Moreover, the analysis result shows better charge separation for 5 wt % in comparison to that of 3 wt % still shows less activity which might be due to agglomeration of MS on the surface of UNH. In addition, time resolved photoluminescence (TRPL) analysis of UNH and (3 wt %) MS/UNH were carried out to study the emission

lifetime of photoexcited electrons as represented in Figure 6f which was fitted to a biexponential model equation:

$$R(t) = A_1 \exp\{-t/\tau_1\} + A_2 \exp\{-t/\tau_2\} \quad (7)$$

where R = normalized emission intensity, t = time after pulsed laser excitation, A = amplitude, and τ = exciton lifetime of individual component. The average lifetime (τ_{avg}) of two exponential decay is indispensable to illustrate the overall TRPL character and can be calculated by eq 8:

$$\tau_{\text{avg}} = \frac{A_1 \tau_1^2 + A_2 \tau_2^2}{A_1 \tau_1 + A_2 \tau_2} \quad (8)$$

where τ_1 and τ_2 are electron-trapping time and formation of electron–hole pairs, respectively.^{42,43} The fluorescence lifetimes were acquired by fitting the decay profile (Table 3) with

Table 3. Exponential-Curve-Fitted TRPL Parameters of UNH and (3 wt %) MS/UNH

sample	τ_1 (ns)	τ_2 (ns)	A_1	A_2	τ_{avg}	χ^2
UNH	0.36	4.81	6600.48	16.40	0.504	1.203
(3 wt %) MS/UNH	0.49	3.21	7947.89	79.25	0.657	1.217

two exponential terms (eq 8). Apparently, the average excited-state lifetime of UNH and (3 wt %) MS/UNH is 0.504 ns (504 ps) and 0.657 ns (657 ps), respectively.^{43,44} The average longer lifetime of (3 wt %) MS/UNH indicates decrease in radiative recombination and increase the lifetime of photo-generated excitons. This investigation further supports the experimental outcomes of the above-mentioned analysis.

5. PHOTOCATALYTIC WATER REDOX REACTION

The synthesized materials were employed toward photocatalytic H_2 and O_2 evolution to evaluate their catalytic efficiency. Pristine UNH has suitable band edge redox potential for the water redox reaction, but it shows only 117.46 $\mu\text{mol/h}$ of H_2 and 61.59 $\mu\text{mol/h}$ of O_2 evolution which might be due to the fast recombination of charge carriers. However, the visible-light-active pristine MS has the suitable VB potential for O_2 evolution and unfavorable CB potential for H_2 evolution. The p–n junction composite, i.e., MS/UNH, shows considerably enhanced consequences due to improved exciton separation. The 3 wt % MS/UNH shows optimum outcome toward H_2 and O_2 evolution, i.e., 512.9 $\mu\text{mol/h}$ (4.37 times greater than bare UNH) and 263.6 $\mu\text{mol/h}$ (4.25 and 11.32 times greater than bare UNH and MS respectively), which can be attributed to high active surface area and inhibition of exciton recombination. Additionally, other composites, i.e., 1 and 5 wt % MS/UNH, generate a relatively smaller amount of product under the same reaction conditions. The decrease in photocatalytic activity for 5 wt % MS/UNH might be due to limited charge separation and aggregation of MS particles on the large surface of UNH that causes a decrease in the area of active sites. In addition, a parallel photocatalytic experiment toward H_2 and O_2 evolution reaction was carried out by physically mixing UNH and MS, i.e., (3 wt %) MS + UNH (physical mixture). The comparative less activity obtained for the physical mixture in comparison to its corresponding composite is mainly due to the physical adsorption by weak van der Waal interactions instead of ionic interfacial interaction between the pristine MS and UNH;

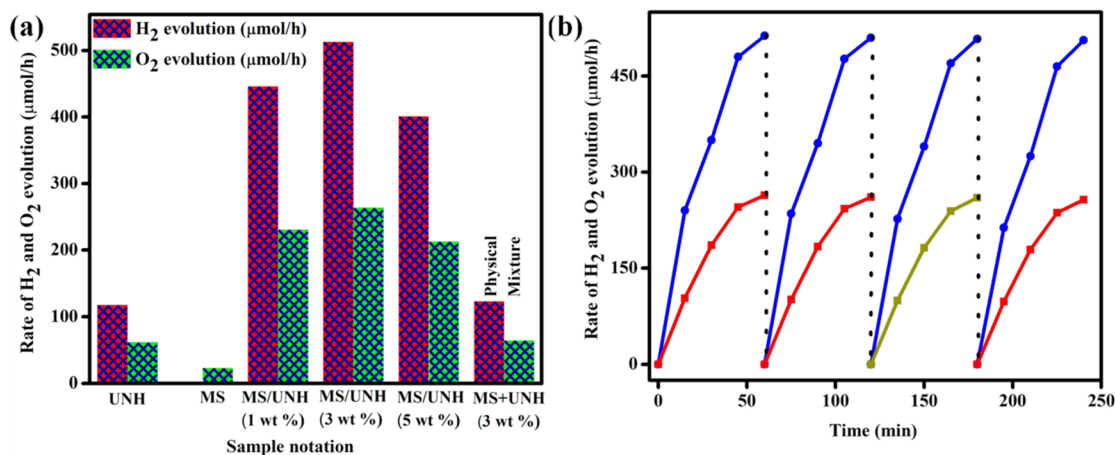


Figure 7. (a) Histograms of H₂ and O₂ production under visible-light irradiation for 1 h. (b) Recyclability study of (3 wt %) MS/UNH toward H₂ and O₂ production.

hence, it shows no synergistic effect. However, hydrothermally prepared composite materials, i.e., (3 wt %) MS/UNH, show comparatively higher activity due to the existence of electrostatic interfacial interaction which provides optimum support toward inhibition of charge recombination by heterojunction interface formation. To validate the photocatalytic capability a comparison analysis table has been provided in Table S1. Furthermore, to verify the photostability, the best photocatalyst, i.e., 3 wt % MS/UNH, was subjected to four consecutive H₂ and O₂ evolution cycles for 1 h each, and the obtained results were depicted in Figure 7b. The conversion efficiency of (3 wt %) MS/UNH toward H₂ and O₂ evolution was estimated by the formula eqs 9–13 as stated below.

5.1. Apparent Conversion Efficiency (ACE) for H₂ Evolution.

$$\Rightarrow \text{ACE} = \frac{\text{stored chemical energy (SCE)}}{\text{incident light intensity (ILI)}} \times 100 \quad (9)$$

$$\Rightarrow \text{ACE} = \frac{\text{moles of H}_2 \text{ produced} \cdot \Delta H_c}{150 \text{ mW cm}^{-2} (\text{spherical surface area on which light falls})} \cdot 100 \quad (10)$$

$$\Rightarrow \frac{512.9 \mu\text{mol/h} \times 285.8 \text{ kJ/mol}}{150 \text{ mW cm}^{-2} \times \pi r^2} \times 100 = \frac{0.04071 \text{ W}}{150 \times 3.141 \times (1.5)^2 \text{ mW cm}^{-2}} \times 100 = 3.84\% \quad (11)$$

5.2. ACE for O₂ Evolution.

$$\Rightarrow \text{ACE} = \frac{\text{moles of O}_2 \text{ produced} \times \Delta H_c}{150 \text{ mW cm}^{-2} \times (\text{spherical surface area on which light falls})} \quad (12)$$

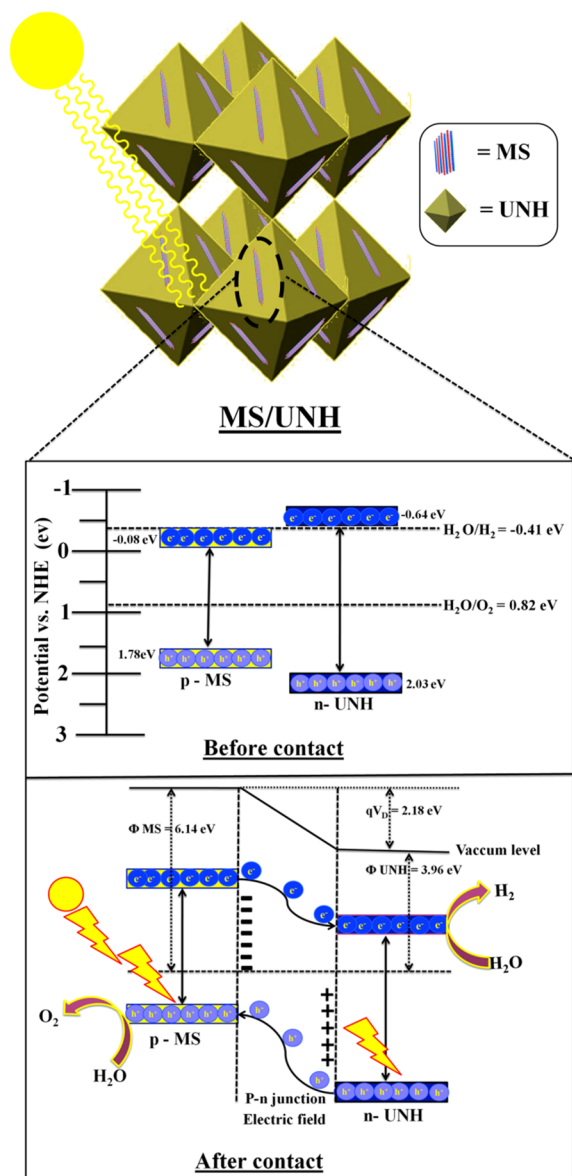
$$\Rightarrow \frac{263.6 \mu\text{mol/h} \times 285.8 \text{ kJ/mol}}{150 \text{ mW cm}^{-2} \times \pi r^2} = \frac{0.02092 \text{ W}}{150 \times 3.141 \times (1.5)^2 \text{ mW cm}^{-2}} = 1.97\% \quad (13)$$

where ΔH_c = combustion heat of H₂ (kJ/mol) [$\text{H}_2\text{O} \rightleftharpoons 2\text{H}^+ + 1/2\text{O}_2$; $\Delta H_c = 285.8 \text{ kJ/mol}$, r = radius of the circle, i.e., 1.5 cm].

6. MECHANISTIC APPROACH

On the basis of characterization analysis outcome, possible photocatalytic mechanistic pathway by MS/UNH toward water redox reaction is depicted in Scheme 2. The excellent photocatalytic efficiency of MS/UNH is due to the comparatively high active surface area (suitable for effective adsorption of adsorbent) and superior exciton separation efficiency (suitable for effective photocatalytic reaction) due to maximum interfacial contact. The high active surface area of UNH in composite is basically responsible for H₂ generation as it contains potential Lewis acid sites (Zr⁴⁺) and base sites (–NH₂), and hence acts as a bifunctional acid–base catalyst. In contrast, water is amphoteric in nature and plays an active role as a Bronsted acid and base. The bifunctional ionic property of UNH provides active sites, i.e., Zr⁴⁺, and sites (–NH₂) for the physisorption of amphoteric water molecule followed by photocatalytic H₂ evolution.⁴⁵ Besides the above-mentioned two factors, the band edge potentials of the respective photocatalyst are one of the crucial prospect from which the accurate mechanistic pathway can be explained. From the UV-DRS and Mott–Schottky analyses, the band edge potentials for UNH were determined to be $E_{\text{VB}} = 2.03 \text{ eV}$ and $E_{\text{CB}} = -0.64 \text{ eV}$, and for MS, they were determined to be $E_{\text{VB}} = 1.78 \text{ eV}$ and $E_{\text{CB}} = -0.08 \text{ eV}$. There are two possible ways of charge transfer by MS/UNH, i.e., (1) double charge transfer and (2) p–n heterojunction to describe the charge flow mechanism toward water redox reaction. In the case of (1) double charge transfer, if the e[−]–h⁺ flow follows this mechanism, then the electron will migrate from the CB of UNH to the CB of MS. At the same time, the migration of the hole takes place from the VB of UNH to the VB of MS resulting in a high charge recombination process. Moreover, the formed potential at the CB of MS is not favorable to reduce water ($\text{H}_2\text{O}/\text{H}_2 = -0.41 \text{ eV}$) due to insufficient standard reduction potential (-0.08 eV). Hence this mechanistic pathway is unfavorable with double charge transfer. Therefore, the second approach, i.e., (ii) p–n heterojunction charge transfer pathway, is more acceptable to describe the redox process and can be explained on the basis of the (a) electronic environment of photosensitized MS/UNH

Scheme 2. Schematic Representation of Proposed p–n Heterojunction Mechanism for Photocatalytic Water Redox Reaction



and (b) role of favorable band edge potential of photocatalyst (MS/UNH) toward photocatalytic water redox reaction.

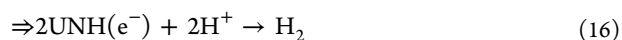
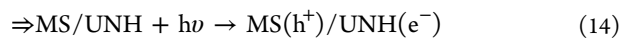
6.1. Electronic Environment of Photosensitized MS/UNH. To determine the mystifying science of heterojunction mechanism, determination of electronic environment of the photocatalyst is very crucial which can be determined from UV–vis, Mott–Schottky, FESEM and XPS analyses. Here the UV–vis analysis of the composite shows favorable band gaps of pristine MS and UNH for heterojunction and proves the visible-light-active property. Next to it, Mott–Schottky analysis result shows p-type behavior of MS and n-type nature of UNH which made them compatible to form a type-II heterojunction type surface contact across the interface, and the coupled structure of MS and UNH shows an inverted V-shape structure, which suggests the p–n type characteristics of the composite is also observed from the potential (I) versus current density (V) graph as shown in Figure 6d. Next, FESEM analysis reveals the nanoflake structure of MS which is a basic

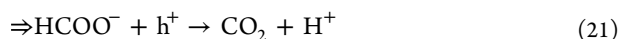
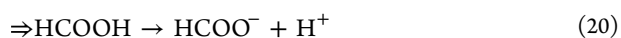
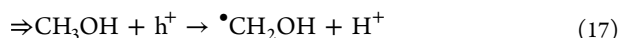
advantage of this analysis, as it will provide maximum interfacial contact toward UNH. Additionally, from XPS analysis the change of electron density provides sufficient evidence toward active species migration, which is only possible due to type-II heterojunction type surface contact across the interface that suppress the active species recombination. Moreover, work functions (Φ), Fermi level (E_f) coalition, and band edge potential are crucial parameters to get in-depth insight of a p–n heterojunction system. In our study, the E_f of MS and UNH was found to be -6.79 and -3.96 , respectively, as presented in Table S2. The carrier density of a semiconductor is inversely proportional to the slope of their Mott–Schottky plot. As is well-observed in the Mott–Schottky study, the composite shows both +ve and –ve shifting for respective counterparts, indicates the downward and upward shifting of the corresponding band edges to make the thermodynamically balanced Fermi level with the formation of a space charge region for the effective separation of exciton pairs. When the Fermi level is thermodynamically balanced, the space charge region exerts force by the captured excitons through a built-in electric field toward the interfacial region of the p–n junction, which effectively enhances the photocatalytic activity of the composite.

The mechanism has been shown in detail in Scheme 2, showing before- and after-contact exciton channelization. Before contact, the electrons and holes will migrate from n-UNH to p-MS and from p-MS to n-UNH, respectively, followed by the formation of a depletion zone between the contact face of MS and UNH. The exciton migration will continue until the occurrence of e^-h^+ equilibrium and that causes band bending by shifting of Fermi level. The band bending creates a built-in potential (2.18 eV) between the contact face to enhance the e^-h^+ separation efficiency. After contact, the exciton channelization occurs in suitably prepared path as projected in Scheme 2. The projected electron–hole channelization inhibits the prospect of recombination and provides suitably active species to get accumulate at respective band edges that served as a commanding tool toward the photocatalytic water redox reaction.

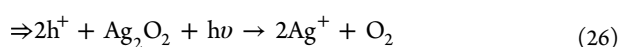
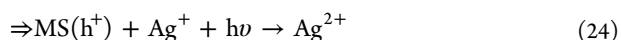
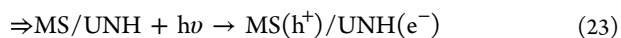
6.2. Role of Favorable Band Edge Potential of Photocatalyst (MS/UNH) toward Photocatalytic Water Redox Reaction. It is well-known that the availability of active species alone is not enough to carry out any photochemical reaction, so the important factor is the reduction potential of band edges at which the excitons are available. In our case, MS exhibited a trace amount of H_2 due to unsuitable band edge potential, whereas the band edge potential of UNH is suitable toward photocatalytic H_2 ($H_2O/H_2 = -0.41$ eV at pH 7) and O_2 ($H_2O/O_2 = 0.82$ eV at pH 7) evolution. After the chemical combination of MS and UNH, the synergistic effect shows the best catalytic performance toward both H_2 ($512.9 \mu\text{mol/h}$) and O_2 ($263.6 \mu\text{mol/h}$) evolution due to suitable band edge potential as well as the least probability of exciton recombination. The water redox reaction (eqs 14–26) has been provided below.

6.2.1. Equation for H_2 Evolution.





6.2.2. Equation for O₂ Evolution.



7. CONCLUSION

Herein we have successfully synthesized a MS/UNH heterojunction hybrid photocatalyst by anchoring nanoflakes MS onto octahedral surface of UNH by an effective hydrothermal route. The observed analysis manifests superior photocatalytic activity toward water redox reaction for the composite in contrast to pristine MS and UNH which is mainly due to an increase in active surface area and maximum interfacial contact that makes available photo-excited charge carriers, owing to the efficient charge separation of electron–hole pairs at suitable band edge potential of the heterojunction compound. The superiority of the active species for the composite is well-supported by EIS spectra, LSV, and transient photo current analyses. Moreover, the hydrophilicity of the –NH₂ group as present in ATA moiety is a most important factor of the enhanced photocatalytic activity. The proposed heterojunction photocatalyst with superior activity, stability, recyclability and excellent photoreceptive nature needs more investigation to explore the full potential of UNH and MS toward energy and the environment.

■ ASSOCIATED CONTENT

SI Supporting Information

The Supporting Information is available free of charge at <https://pubs.acs.org/doi/10.1021/acs.inorgchem.0c01030>.

Characterization and FTO preparation, FESEM and HRTEM spectrogram of MS, EDAX OF MS/UNH (3 wt %), color mapping of Zr, C, N, O, Mo, and S for MS/UNH, PL spectrogram of UNH and MS/UNH (1, 3, and 5 wt %), Mott schottky spectrogram of MS, comparative analysis of H₂ evolution, calculation of Fermi level and build in potential (PDF)

■ AUTHOR INFORMATION

Corresponding Author

Kulamani Parida – Centre for Nanoscience and Nanotechnology, Siksha ‘O’ Anusandhan (Deemed to be University), Bhubaneswar, Odisha 751030, India;
 orcid.org/0000-0001-7807-5561; Phone: +91-674-2351777; Email: paridakulamani@yahoo.com, kulamani@soa.ac.in; Fax: +91-674-2350642

Authors

Satyabrata Subudhi – Centre for Nanoscience and Nanotechnology, Siksha ‘O’ Anusandhan (Deemed to be University), Bhubaneswar, Odisha 751030, India

Gayatri Swain – Centre for Nanoscience and Nanotechnology, Siksha ‘O’ Anusandhan (Deemed to be University), Bhubaneswar, Odisha 751030, India

Suraj Prakash Tripathy – Centre for Nanoscience and Nanotechnology, Siksha ‘O’ Anusandhan (Deemed to be University), Bhubaneswar, Odisha 751030, India

Complete contact information is available at:

<https://pubs.acs.org/10.1021/acs.inorgchem.0c01030>

Notes

The authors declare no competing financial interest.

■ ACKNOWLEDGMENTS

The authors are very thankful to the Siksha ‘O’ Anusandhan (Deemed to be University) management for their encouragement and constant support.

■ REFERENCES

- (1) Shi, J.; Ye, J.; Ma, L.; Ouyang, S.; Jing, D.; Guo, L. Site-Selected Doping of Upconversion Luminescent Er³⁺ into SrTiO₃ for Visible-Light-Driven Photocatalytic H₂ or O₂ Evolution. *Chem. - Eur. J.* **2012**, *18*, 7543–7551.
- (2) Maeda, K.; Hashiguchi, H.; Masuda, H.; Abe, R.; Domen, K. Photocatalytic Activity of (Ga_{1-x}Zn_x)(N_{1-x}O_x) for Visible-Light-Driven H₂ and O₂ Evolution in the Presence of Sacrificial Reagents. *J. Phys. Chem. C* **2008**, *112*, 3447–3452.
- (3) Niishiro, R.; Tanaka, S.; Kudo, A. Hydrothermal-Synthesized SrTiO₃ Photocatalyst Codoped with Rhodium and Antimony with Visible-Light Response for Sacrificial H₂ and O₂ Evolution and Application to Overall Water Splitting. *Appl. Catal., B* **2014**, *150–151*, 187–196.
- (4) Zhao, J.; Wang, X.; Xu, Z.; Loo, J. S. C. Hybrid Catalysts for Photoelectrochemical Reduction of Carbon Dioxide: A Prospective Review on Semiconductor/Metal Complex Co-Catalyst Systems. *J. Mater. Chem. A* **2014**, *2*, 15228.
- (5) Paramanik, L.; Reddy, K. H.; Parida, K. M. An Energy Band Compactable B-RGO/PbTiO₃ p–n Junction: A Highly Dynamic and Durable Photocatalyst for Enhanced Photocatalytic H₂ Evolution. *Nanoscale* **2019**, *11*, 22328–22342.
- (6) Li, J.; Wang, H.; Yuan, X.; Zhang, J.; Chew, J. W. Metal-organic framework membranes for wastewater treatment and water regeneration. *Coord. Chem. Rev.* **2020**, *404*, 213116.
- (7) Dong, W.; Wang, D.; Wang, H.; Li, M.; Chen, F.; Jia, F.; Yang, Q.; Li, X.; Yuan, X.; Gong, J.; Li, H.; Ye, J. Facile synthesis of In₂S₃/UiO-66 composite with enhanced adsorption performance and photocatalytic activity for the removal of tetracycline under visible light irradiation. *J. Colloid Interface Sci.* **2019**, *535*, 444–457.
- (8) Subudhi, S.; Rath, D.; Parida, K. M. A Mechanistic Approach towards the Photocatalytic Organic Transformations over Functionalised Metal Organic Frameworks: A Review. *Catal. Sci. Technol.* **2018**, *8*, 679–696.
- (9) Barthelet, K.; Marrot, J.; Riou, D.; Férey, G. A Breathing Hybrid Organic–Inorganic Solid with Very Large Pores and High Magnetic Characteristics. *Angew. Chem., Int. Ed.* **2002**, *41*, 281.
- (10) Serre, C.; Millange, F.; Thouvenot, C.; Noguès, M.; Marsolier, G.; Louër, D.; Férey, G. Very Large Breathing Effect in the First Nanoporous Chromium(III)-Based Solids: MIL-53 or Cr^{III}(OH)·{O₂C–C₆H₄–CO₂}·{HO₂C–C₆H₄–CO₂H}_x·H₂O. *J. Am. Chem. Soc.* **2002**, *124*, 13519–13526.
- (11) Cui, Y.; Yue, Y.; Qian, G.; Chen, B. Luminescent Functional Metal–Organic Frameworks. *Chem. Rev.* **2012**, *112*, 1126–1162.

- (12) Asahi, R. Visible-Light Photocatalysis in Nitrogen-Doped Titanium Oxides. *Science (Washington, DC, U. S.)* **2001**, *293*, 269–271.
- (13) Khan, S. U. M. Efficient Photochemical Water Splitting by a Chemically Modified N-TiO₂. *Science* **2002**, *297*, 2243–2245.
- (14) Dvoranová, D.; Brezová, V.; Mazúr, M.; Malati, M. A. Investigations of Metal-Doped Titanium Dioxide Photocatalysts. *Appl. Catal., B* **2002**, *37*, 91–105.
- (15) Chen, X.; Li, C.; Grätzel, M.; Kostecki, R.; Mao, S. S. Nanomaterials for Renewable Energy Production and Storage. *Chem. Soc. Rev.* **2012**, *41*, 7909.
- (16) Linic, S.; Christopher, P.; Ingram, D. B. Plasmonic-Metal Nanostructures for Efficient Conversion of Solar to Chemical Energy. *Nat. Mater.* **2011**, *10*, 911–921.
- (17) Fang, J.; Xu, L.; Zhang, Z.; Yuan, Y.; Cao, S.; Wang, Z.; Yin, L.; Liao, Y.; Xue, C. Au@TiO₂ – CdS Ternary Nanostructures for Efficient Visible-Light-Driven Hydrogen Generation. *ACS Appl. Mater. Interfaces* **2013**, *5*, 8088–8092.
- (18) Cao, S.-W.; Fang, J.; Shahjamali, M. M.; Boey, F. Y. C.; Barber, J.; Loo, S. C. J.; Xue, C. Plasmon-Enhanced Hydrogen Evolution on Au-InVO₄ Hybrid Microspheres. *RSC Adv.* **2012**, *2*, 5513.
- (19) Gomes Silva, C.; Luz, I.; Llabrés i Xamena, F. X.; Corma, A.; García, H. Water Stable Zr-Benzenedicarboxylate Metal-Organic Frameworks as Photocatalysts for Hydrogen Generation. *Chem. - Eur. J.* **2010**, *16*, 11133–11138.
- (20) Wang, C.; DeKrafft, K. E.; Lin, W. Pt Nanoparticles@Photoactive Metal–Organic Frameworks: Efficient Hydrogen Evolution via Synergistic Photoexcitation and Electron Injection. *J. Am. Chem. Soc.* **2012**, *134*, 7211–7214.
- (21) Kataoka, Y.; Sato, K.; Miyazaki, Y.; Masuda, K.; Tanaka, H.; Naito, S.; Mori, W. Photocatalytic Hydrogen Production from Water Using Porous Material [Ru₂(p-BDC)₂]N. *Energy Environ. Sci.* **2009**, *2*, 397.
- (22) Subudhi, S.; Mansingh, S.; Swain, G.; Behera, A.; Rath, D.; Parida, K. HPW-Anchored UiO-66 Metal–Organic Framework: A Promising Photocatalyst Effective toward Tetracycline Hydrochloride Degradation and H₂ Evolution via Z-Scheme Charge Dynamics. *Inorg. Chem.* **2019**, *58*, 4921–4934.
- (23) Voiry, D.; Mohite, A.; Chhowalla, M. Phase Engineering of Transition Metal Dichalcogenides. *Chem. Soc. Rev.* **2015**, *44*, 2702–2712.
- (24) Kumar, N. A.; Dar, M. A.; Gul, R.; Baek, J. B. Graphene and Molybdenum Disulfide Hybrids: Synthesis and Applications. *Mater. Today* **2015**, *18*, 286–298.
- (25) Liu, T.; Shi, S.; Liang, C.; Shen, S.; Cheng, L.; Wang, C.; Song, X.; Goel, S.; Barnhart, T. E.; Cai, W.; Liu, Z. Iron Oxide Decorated MoS₂ Nanosheets with Double PEGylation for Chelator-Free Radiolabeling and Multimodal Imaging Guided Photothermal Therapy. *ACS Nano* **2015**, *9*, 950–960.
- (26) Swain, G.; Sultana, S.; Parida, K. One-Pot-Architected Au-Nanodot-Promoted MoS₂/ZnIn₂S₄: A Novel p–n Heterojunction Photocatalyst for Enhanced Hydrogen Production and Phenol Degradation. *Inorg. Chem.* **2019**, *58*, 9941–9955.
- (27) Nayak, S.; Swain, G.; Parida, K. Enhanced Photocatalytic Activities of RhB Degradation and H₂ Evolution from in Situ Formation of the Electrostatic Heterostructure MoS₂/NiFe LDH Nanocomposite through the Z-Scheme Mechanism via p–n Heterojunctions. *ACS Appl. Mater. Interfaces* **2019**, *11*, 20923–20942.
- (28) Hao, X.; Jin, Z.; Yang, H.; Lu, G.; Bi, Y. Peculiar synergistic effect of MoS₂ quantum dots and graphene on Metal-Organic Frameworks for photocatalytic hydrogen evolution. *Appl. Catal., B* **2017**, *210*, 45–56.
- (29) Shen, L.; Luo, M.; Liu, Y.; Liang, R.; Jing, F.; Wu, L. Noble-metal-free MoS₂ co-catalyst decorated UiO-66/CdS hybrids for efficient photocatalytic H₂ production. *Appl. Catal., B* **2015**, *166*, 445–453.
- (30) Subudhi, S.; Mansingh, S.; Tripathy, S. P.; Mohanty, A.; Mohapatra, P.; Rath, D.; Parida, K. The Fabrication of Au/Pd Plasmonic Alloys on UiO-66-NH₂: An Efficient Visible Light-Induced Photocatalyst towards the Suzuki Miyaura Coupling Reaction under Ambient Conditions. *Catal. Sci. Technol.* **2019**, *9*, 6585–6597.
- (31) Zhou, K.; Liu, J.; Wang, B.; Zhang, Q.; Shi, Y.; Jiang, S.; Hu, Y.; Gui, Z. Facile Preparation of Poly(Methyl Methacrylate)/MoS₂ Nanocomposites via in Situ Emulsion Polymerization. *Mater. Lett.* **2014**, *126*, 159–161.
- (32) Naresh Kumar, T.; Chandrasekaran, N.; Lakshminarasimha Phani, K. Structural and Electronic Modification of MoS₂ Nanosheets Using S-Doped Carbon for Efficient Electrocatalysis of the Hydrogen Evolution Reaction. *Chem. Commun.* **2015**, *51*, 5052–5055.
- (33) Ye, R.; Fang, H.; Zheng, Y. Z.; Li, N.; Wang, Y.; Tao, X. Fabrication of CoTiO₃/g-C₃N₄ hybrid photocatalysts with enhanced H₂ evolution: Z-scheme photocatalytic mechanism insight. *ACS Appl. Mater. Interfaces* **2016**, *8*, 13879–13889.
- (34) Su, Y.; Zhang, Z.; Liu, H.; Wang, Y. Cd_{0.2}Zn_{0.8}S@UiO-66-NH₂ Nanocomposites as Efficient and Stable Visible-Light-Driven Photocatalyst for H₂ Evolution and CO₂ Reduction. *Appl. Catal., B* **2017**, *200*, 448–457.
- (35) Wang, Y.; Wang, L.; Huang, W.; Zhang, T.; Hu, X.; Perman, J. A.; Ma, S. A Metal–Organic Framework and Conducting Polymer Based Electrochemical Sensor for High Performance Cadmium Ion Detection. *J. Mater. Chem. A* **2017**, *5*, 8385–8393.
- (36) Shen, L.; Wu, W.; Liang, R.; Lin, R.; Wu, L. Highly Dispersed Palladium Nanoparticles Anchored on UiO-66(NH₂) Metal-Organic Framework as a Reusable and Dual Functional Visible-Light-Driven Photocatalyst. *Nanoscale* **2013**, *5*, 9374.
- (37) Hao, X.; Jin, Z.; Yang, H.; Lu, G.; Bi, Y. Peculiar Synergistic Effect of MoS₂ Quantum Dots and Graphene on Metal-Organic Frameworks for Photocatalytic Hydrogen Evolution. *Appl. Catal., B* **2017**, *210*, 45–56.
- (38) Subudhi, S.; Paramanik, L.; Sultana, S.; Mansingh, S.; Mohapatra, P.; Parida, K. A Type-II Interband Alignment Heterojunction Architecture of Cobalt Titanate Integrated UiO-66-NH₂: A Visible Light Mediated Photocatalytic Approach Directed towards Norfloxacin Degradation and Green Energy (Hydrogen) Evolution. *J. Colloid Interface Sci.* **2020**, *568*, 89–105.
- (39) Zhang, X.; Dong, H.; Sun, X. J.; Yang, D. D.; Sheng, J. L.; Tang, H. L.; Meng, X. B.; Zhang, F. M. Step-by-Step Improving Photocatalytic Hydrogen Evolution Activity of NH₂-UiO-66 by Constructing Heterojunction and Encapsulating Carbon Nanodots. *ACS Sustainable Chem. Eng.* **2018**, *6*, 11563–11569.
- (40) Shen, L.; Wu, W.; Liang, R.; Lin, R.; Wu, L. Highly dispersed palladium nanoparticles anchored on UiO-66 (NH₂) metal-organic framework as a reusable and dual functional visible-light-driven photocatalyst. *Nanoscale* **2013**, *5*, 9374–9382.
- (41) Wang, H.; Qian, C.; Liu, J.; Zeng, Y.; Wang, D.; Zhou, W.; Gu, L.; Wu, H.; Liu, G.; Zhao, Y. Integrating Suitable Linkage of Covalent Organic Frameworks into Covalently Bridged Inorganic/Organic Hybrids toward Efficient Photocatalysis. *J. Am. Chem. Soc.* **2020**, *142*, 4862–4871.
- (42) Nayak, S.; Mohapatra, L.; Parida, K. Visible light-driven novel g-C₃N₄/NiFe-LDH composite photocatalyst with enhanced photocatalytic activity towards water oxidation and reduction reaction. *J. Mater. Chem. A* **2015**, *3*, 18622–18635.
- (43) Tian, P.; He, X.; Zhao, L.; Li, W.; Fang, W.; Chen, H.; Zhang, F.; Huang, Z.; Wang, H. Enhanced charge transfer for efficient photocatalytic H₂ evolution over UiO-66-NH₂ with annealed Ti₃C₂T_x MXenes. *Int. J. Hydrogen Energy* **2019**, *44*, 788–800.
- (44) Xiao, J. D.; Shang, Q.; Xiong, Y.; Zhang, Q.; Luo, Y.; Yu, S. H.; Jiang, H. L. Boosting photocatalytic hydrogen production of a metal-organic framework decorated with platinum nanoparticles: The platinum location matters. *Angew. Chem., Int. Ed.* **2016**, *55*, 9389–9393.
- (45) Yang, Y.; Yao, H. F.; Xi, F. G.; Gao, E. Q. Amino-functionalized Zr (IV) metal–organic framework as bifunctional acid–base catalyst for Knoevenagel condensation. *J. Mol. Catal. A: Chem.* **2014**, *390*, 198–205.